

Order parameter with line nodes and s_{\pm} -wave symmetry for the noncentrosymmetric superconductor $\text{Li}_2\text{Pt}_3\text{B}$

Soumya P. Mukherjee¹ and Tetsuya Takimoto^{1,2}¹*Asia Pacific Center for Theoretical Physics, Hogil Kim Memorial Building 5th Floor, POSTECH, Hyoja-dong, Namgu, Pohang 790-784, Republic of Korea*²*Department of Physics, POSTECH, Pohang, Gyeongbuk 790-784, Republic of Korea*

(Received 10 October 2011; revised manuscript received 21 September 2012; published 23 October 2012)

The nature and symmetry of the superconducting gap function in the noncentrosymmetric superconductor $\text{Li}_2\text{Pt}_3\text{B}$, even many years after its discovery, appear to be full of contradictions. In this article based on the existing band structure calculations we find that owing to the considerable nesting near the Fermi surface and the enhanced d character of the relevant bands that cross the Fermi level, the system gets weakly correlated. Considering the effect of the on-site Coulomb repulsion on the pairing potential perturbatively, we extract a possible superconducting transition. The strong normal spin fluctuation gives rise to a singlet-dominant gap function with accompanying sign change. Thus our theory predicts an s_{\pm} -wave gap function with line nodes as the most promising candidate in the superconducting state.

DOI: [10.1103/PhysRevB.86.134526](https://doi.org/10.1103/PhysRevB.86.134526)

PACS number(s): 74.20.Mn, 74.20.Rp, 74.70.-b, 74.90.+n

I. INTRODUCTION

Unconventional superconductivity appears in the correlated electron system, where electron correlation plays a role in producing an effective pairing potential. Here, Cooper pairs are formed by electrons sited on different sites. On the other hand, the conventional s -wave superconductivity mediated by the phonon between electrons at the same site principally is considerably suppressed due to the local electron Coulomb repulsion. The fact that the momentum summation of the order parameter of superconductivity in the first Brillouin zone vanishes is a feature of unconventional superconductivity, since the symmetry of unconventional superconductivity is different from that of the conventional s -wave superconductivity. Actually, these features are observed in well-known unconventional superconductors, such as high- T_c cuprate^{1,2} and heavy-fermion superconductors.³⁻⁵

The discovery of superconductivity in the noncentrosymmetric compound CePt_3Si ⁶ opened a new field of research. Broken inversion symmetry gives rise to an antisymmetric spin-orbit coupling which splits the spin degenerate electronic bands into two, each of which are now described by a helicity index. Gor'kov and Rashba⁷ already predicted that the superconducting order parameter in such a system is bound to be a mixture of spin-singlet as well as spin-triplet components. On the other hand, this gives rise to many unusual behaviors which are revealed through various experiments. Many possible theoretical explanations came up to explain these behaviors. These anomalous behaviors include high upper critical field,⁸⁻¹⁰ large residual susceptibility and its anisotropy,¹¹⁻¹³ properties related to the Josephson junction and different tunnel junctions,¹⁴⁻¹⁸ impurity effects,¹⁹⁻²² the existence of edge states,²³⁻²⁵ the possibility of finding Majorana fermions,²⁶ and very recently their novel topological aspects.²⁷⁻³² The mixed-parity pairing state could be realized by a peculiar mechanism capturing features of the noncentrosymmetric system.³³⁻³⁵ For CePt_3Si the fact that the superconducting phase coexists with the magnetic phase⁶ makes it difficult to clarify the mechanism. Presently many

other noncentrosymmetric superconductors have been found in the extensive investigation.

The experimental finding of superconductivity in $\text{Li}_2\text{Pd}_3\text{B}$ ³⁶ and subsequently the experiments in the pseudobinary complete solid solution $\text{Li}_2(\text{Pd}_{1-x}\text{Pt}_x)_3\text{B}$, $x = 0 \sim 1$,³⁷ attracted much attention as the superconducting phase for this family of compounds does not coexist with other phases. This makes the system simple for studying the properties of noncentrosymmetric superconductors (NCSs). There exist many experimental as well as theoretical works reporting different interesting aspects of this family of compounds. The end compounds $\text{Li}_2\text{Pd}_3\text{B}$ ($x = 0$) and $\text{Li}_2\text{Pt}_3\text{B}$ ($x = 1$)³⁸⁻⁴³ were also studied intensively and compared. It is now established that the superconductivity in $\text{Li}_2\text{Pd}_3\text{B}$ is of the phonon-mediated s -wave type.⁴⁴ The presence of the Hebel-Slichter peak in the nuclear spin-lattice relaxation rate measurement,^{38,39} low-temperature behavior of the specific heat,^{40,41} penetration depth,⁴³ etc., as well as NMR Knight shift data strongly support this conclusion. On the other hand, the nature and symmetry of the gap function of the compound $\text{Li}_2\text{Pt}_3\text{B}$ is still debatable. According to similar experiments on this compound^{39,41,43} the presence of line nodes is suggested, indicating some unconventional superconducting state. The NMR Knight shift, often used to distinguish the spin state of the Cooper pair between singlet and triplet, is almost temperature independent even below T_c . This behavior is also interesting and deserves special attention.

The article is organized as follows. In Sec. II based on the existing band structure calculations^{45,46} we derive an effective band model which captures the essential features of the band structure calculations. We establish a nesting between two branches of the Fermi surface by calculating the interband as well as intraband static susceptibilities. We further calculate the static charge and spin susceptibilities numerically and estimate the effect of different spin fluctuations. Here we would like to mention that earlier work⁴⁷ which aimed to explain this compound did not consider these effects. In Sec. III we derive the superconducting gap equation within the weak-coupling approach by estimating the pairing potential

within the perturbation theory for the electron repulsion. From the momentum dependencies of the pairing potential it is clear that owing to the large usual spin fluctuation the singlet gap function becomes much stronger than the triplet gap function. We then solve the gap equations numerically and find the detailed nature of the gap function. We find that the gap function belongs to the A_1 representation of the corresponding point group with sign change between two branches of the Fermi surface. Thus our theory suggests a singlet-dominant s_{\pm} -wave gap function with line nodes on another branch of the Fermi surface as the most promising candidate for the superconducting state of $\text{Li}_2\text{Pt}_3\text{B}$. This prediction also explains most of the experiments, suggesting the existence of the line node. We then discuss the structure of the line nodes and the possibility of getting zero-energy surface bound states in Sec. IV. Finally in Sec. V we calculate the behavior of uniform spin susceptibility below T_c . We also draw conclusions from our work and suggest some experiments to facilitate further investigation.

II. MODEL HAMILTONIAN FOR $\text{Li}_2\text{Pt}_3\text{B}$

In this section we present the model Hamiltonian for the noncentrosymmetric superconductor $\text{Li}_2\text{Pt}_3\text{B}$ and reveal the important role of nesting between different branches of the Fermi surface based on the evidences of the existing literature. The crystal structure of the compound $\text{Li}_2\text{Pt}_3\text{B}$ is simple cubic (with point group O) and isostructural with the compound $\text{Li}_2\text{Pd}_3\text{B}$. The only difference between them is in the mass of the central Pt and Pd atoms. However this gives rise to some significant observable effects.^{45,46} For the Pt compound there is an enhancement of the d character of the bands that cross the Fermi level. This enhancement of the d character is reflected in the increased density of state at the Fermi level. Considering these, we consider a minimal model Hamiltonian ($H = H_0 + H_1$) of $\text{Li}_2\text{Pt}_3\text{B}$ which is given by the Hubbard model with an antisymmetric spin-orbit (ASO) coupling term, where

$$H_0 = \sum_{\mathbf{k}\sigma\sigma'} ([\varepsilon_{\mathbf{k}} - \mu] \hat{\sigma}_o + \mathbf{g}_{\mathbf{k}} \cdot \hat{\sigma})_{\sigma\sigma'} c_{\mathbf{k}\sigma}^\dagger c_{\mathbf{k}\sigma'}, \quad (1)$$

$$H_1 = U \sum_i n_{i\uparrow} n_{i\downarrow}. \quad (2)$$

Here $c_{\mathbf{k}\sigma}$ and $c_{\mathbf{k}\sigma}^\dagger$ denote the annihilation and creation operators of an electron with momentum \mathbf{k} and spin σ . $\varepsilon_{\mathbf{k}}$ is the dispersion of electrons and μ the chemical potential. $\mathbf{g}_{\mathbf{k}} = -\mathbf{g}_{-\mathbf{k}}$ denotes the effective ASO coupling which breaks the inversion symmetry. Thus H_0 describes the usual noncentrosymmetric metallic system. In the interaction term H_1 , U is the strength of the screened on-site interaction.

Now we concentrate on the main features of the electronic bands near the Fermi level for the compound $\text{Li}_2\text{Pt}_3\text{B}$, obtained by the previous first-principles calculations.^{45,46} A careful study of these works suggests that the major contribution to the density of states comes from Pt $5d$ bands. These d bands cross the Fermi level forming discrete Fermi surfaces. We can clearly identify electron pockets at the Γ and M points and hole pockets at the R and X points. Also the electron pocket at the Γ point is connected to the hole pockets at the R point by

a nesting vector (π, π, π) which is half of the reciprocal lattice vector.

Based on the discussions in the previous paragraph, we give an effective band which captures most of these essential features. The dispersion of electrons $\varepsilon_{\mathbf{k}}$ is described by the tight-binding method including up to fourth-neighbor hopping in the three-dimensional simple cubic lattice:

$$\begin{aligned} \varepsilon_{\mathbf{k}} = & 2t_1[\cos(k_x) + \cos(k_y) + \cos(k_z)] \\ & + 4t_2[\cos(k_x)\cos(k_y) + \cos(k_y)\cos(k_z) \\ & + \cos(k_z)\cos(k_x)] + 8t_3\cos(k_x)\cos(k_y)\cos(k_z) \\ & + 2t_4[\cos(2k_x) + \cos(2k_y) + \cos(2k_z)]. \end{aligned} \quad (3)$$

The ASO coupling term appropriate for the point group is given as $\mathbf{g}_{\mathbf{k}} = g(\sin(k_x), \sin(k_y), \sin(k_z))$. Here g indicates the strength of the ASO coupling. The values of the parameters $(t_1, t_2, t_3, t_4, g, \mu)$ are chosen to be $(1.0, -0.03, -0.88, -0.03, 0.5, 0.02)$ as Fermi surfaces obtained by the band structure calculation are reproduced. One can diagonalize H_0 to get the eigenenergies $\varepsilon_{\mathbf{k}\pm} = \varepsilon_{\mathbf{k}} \pm |\mathbf{g}_{\mathbf{k}}| - \mu$, which give us the energy of the two helicity bands. The Fermi surfaces of the two opposite helicity bands as obtained by the fitting are shown in Fig. 1. From the figure it is clear that the Fermi surfaces for both helically split bands consist of three major branches: one small electron pocket around the Γ point, hole pockets around the R points, and the other remaining large portion forming a cagelike structure with neck and mouth along the Γ -X directions. The corresponding parts of the Fermi surfaces of the different helicity bands are shifted from each other depending on the magnitude of g . Owing to the smallness of the parameters t_2, t_4 , and μ there appears a large nesting with a vector $\mathbf{Q} = (\pi, \pi, \pi)$ connecting between the cagelike portion of the Fermi surface of the negative helicity band $\varepsilon_{\mathbf{k}-}$ and the similar Fermi surface of the positive helicity band $\varepsilon_{\mathbf{k}+}$.

The presence of this nesting is also verified in the momentum dependence of the interband susceptibility $\chi_{+-}(\mathbf{q})$. By definition $\chi_{\eta\xi}(\mathbf{q})$ is given as

$$\chi_{\eta\xi}(\mathbf{q}) = \frac{1}{8N_0} \sum_{\mathbf{k}} \frac{f(\varepsilon_{\mathbf{k}\xi}) - f(\varepsilon_{\mathbf{k}+\mathbf{q}\eta})}{\varepsilon_{\mathbf{k}+\mathbf{q}\eta} - \varepsilon_{\mathbf{k}\xi}}, \quad (4)$$

where $\eta, \xi = \pm$. Here $f(\varepsilon_{\mathbf{k}\xi})$ is the Fermi function and $\varepsilon_{\mathbf{k}\xi}$ is the dispersion relation of the helicity bands. We thus calculate the momentum dependence of all $\chi_{\eta\xi}(\mathbf{q})$ and plot them in Fig. 2. As expected, we observe a sharp peak at the R point indicating the (π, π, π) nesting in the momentum dependence of $\chi_{+-}(\mathbf{q})$, as shown by the red dotted line in Fig. 2. We also observe peaks near the nesting vector $\mathbf{Q} = (\pi, \pi, \pi)$ in the momentum dependence of both $\chi_{++}(\mathbf{q})$ and $\chi_{--}(\mathbf{q})$. This indicates the fact that there also exists partial intraband nesting as well. This nesting will occur between the Fermi surfaces around the Γ and R points of both helicity bands.

In the remaining part of this section we examine the effect of nesting in the static susceptibilities $\chi_{\alpha\beta}$ where α and β are either a component of spin \mathbf{S} or a charge component. As we see later the superconducting pairing potential is described by the static susceptibility $\chi_{\alpha\beta}(\mathbf{q})$. We calculate the momentum dependence of all susceptibility components numerically for the cubic NCS system and examine the property of spin fluctuations. The dynamical susceptibility tensor is

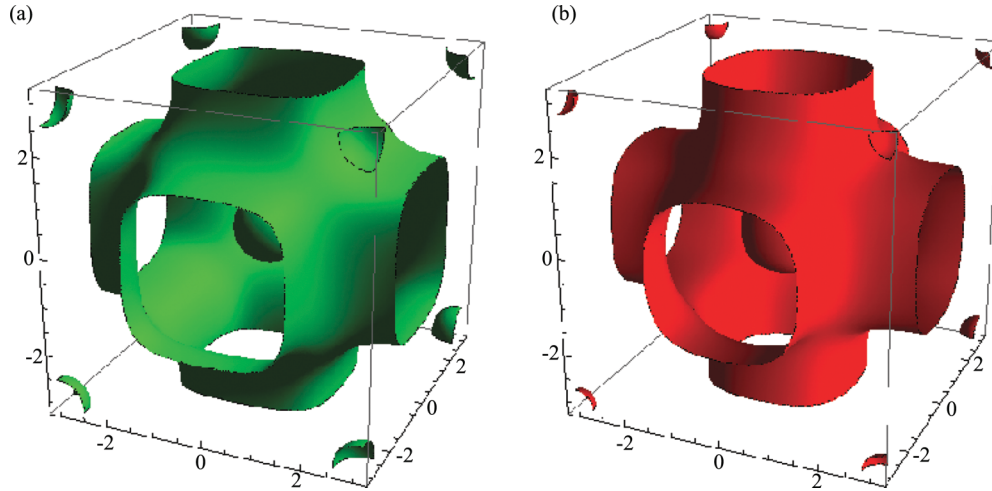


FIG. 1. (Color online) Different branches of the Fermi surfaces for (a) positive helicity band and (b) negative helicity band. Both the Fermi surfaces consist of central spherical part around the Γ point and another branch at the R points. The remaining part forms a cage-like structure. The cage-like Fermi surfaces for two helicity bands overlap with each other when translated by the nesting vector $\mathbf{Q} = (\pi, \pi, \pi)$. Details are described in text.

defined as

$$\chi_{\alpha\beta}(\mathbf{q}, i\Omega_n) = \int_0^{1/T} d\tau e^{i\Omega_n\tau} \langle T_{\tau} [S_{\mathbf{q}}^{\alpha}(\tau) S_{-\mathbf{q}}^{\beta}(0)] \rangle. \quad (5)$$

Here $\langle \dots \rangle$ denotes thermal average, T_{τ} imaginary time ordering, and Ω_n are the bosonic Matsubara frequencies. The charge ($\alpha = c$) and τ component of spin ($\alpha = \tau$) operators with wave vector \mathbf{q} are defined as

$$S_{\mathbf{q}}^c = \frac{1}{2} \sum_{\mathbf{k}\sigma} c_{\mathbf{k}\sigma}^{\dagger} c_{\mathbf{k}+\mathbf{q}\sigma}, \quad S_{\mathbf{q}}^{\tau} = \frac{1}{2} \sum_{\mathbf{k}\sigma\sigma'} \sigma_{\sigma\sigma'}^{\tau} c_{\mathbf{k}\sigma}^{\dagger} c_{\mathbf{k}+\mathbf{q}\sigma'}, \quad (6)$$

where σ^{τ} is the τ component of the Pauli matrix ($\tau = x, y, z$). Simultaneously with Eq. (4) using Eqs. (5) and (6) we arrive at the momentum dependencies of the matrix elements of the

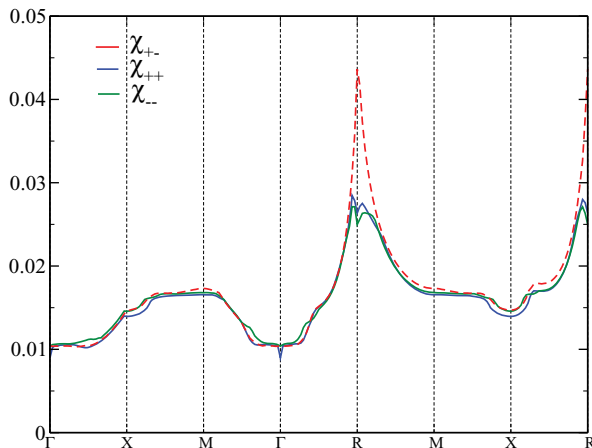


FIG. 2. (Color online) Signature of nesting. Momentum dependence of interband and intraband susceptibilities showing nesting around $\mathbf{Q} = (\pi, \pi, \pi)$.

static spin susceptibilities $\chi_{\tau\tau'}(\mathbf{q})$ in the noninteracting case $U = 0$:

$$\chi_{\tau\tau'}(\mathbf{q}) = \frac{1}{8N_0} \sum_{\mathbf{k}} \sum_{\xi\xi'} \Gamma_{\xi\xi'}^{\tau\tau'}(\mathbf{k}; \mathbf{q}) \frac{f(\varepsilon_{\mathbf{k}\xi}) - f(\varepsilon_{\mathbf{k}+\mathbf{q}\xi})}{\varepsilon_{\mathbf{k}+\mathbf{q}\xi} - \varepsilon_{\mathbf{k}\xi}}, \quad (7)$$

where $f(\varepsilon)$ is the Fermi distribution function and the function $\Gamma_{\xi\xi'}^{\tau\tau'}$ is obtained as

$$\Gamma_{\xi\xi'}^{\tau\tau'}(\mathbf{k}; \mathbf{q}) = \delta_{\tau,\tau'} (1 - \xi\xi' \tilde{\mathbf{g}}_{\mathbf{k}} \cdot \tilde{\mathbf{g}}_{\mathbf{k}+\mathbf{q}}) + \xi\xi' (\tilde{\mathbf{g}}_{\mathbf{k}\tau} \tilde{\mathbf{g}}_{\mathbf{k}+\mathbf{q}\tau'} + \tilde{\mathbf{g}}_{\mathbf{k}\tau'} \tilde{\mathbf{g}}_{\mathbf{k}+\mathbf{q}\tau}) - \epsilon_{\tau\tau'\tau''} i (\xi \tilde{\mathbf{g}}_{\mathbf{k}+\mathbf{q}\tau''} - \xi' \tilde{\mathbf{g}}_{\mathbf{k}\tau''}). \quad (8)$$

Here $\tilde{\mathbf{g}}_{\mathbf{k}\tau}$ is the direction cosines along the τ direction and $\epsilon_{\tau\tau'\tau''}$ is the usual Levi-Civita symbols where τ, τ', τ'' denote spatial indices. Similarly the charge fluctuation in the normal state, i.e., $\chi_{cc}(\mathbf{q})$, is obtained with the replacement of $\Gamma_{\xi\xi'}^{\tau\tau'}(\mathbf{k}; \mathbf{q})$ by $\Gamma_{\xi\xi'}^{cc}(\mathbf{k}; \mathbf{q})$ where $\Gamma_{\xi\xi'}^{cc}(\mathbf{k}; \mathbf{q}) = 1 + \xi\xi' \tilde{\mathbf{g}}_{\mathbf{k}} \cdot \tilde{\mathbf{g}}_{\mathbf{k}+\mathbf{q}}$. The susceptibilities between spin and charge operators $\chi_{c\tau}(\mathbf{q})$ and $\chi_{\tau c}(\mathbf{q})$ all vanish for the static case. All other susceptibility components have different momentum dependence.

We further consider the contributions of nesting to different spin fluctuations. According to the group theoretical consideration,³⁴ the symmetry of momentum dependence of every spin susceptibility could be classified as follows. The usual spin fluctuation $\frac{1}{3}(\chi_{xx} + \chi_{yy} + \chi_{zz})$ which is also present in the centrosymmetric cubic system has the momentum dependence of q^2 type. Other symmetric spin fluctuations $(2\chi_{zz} - \chi_{xx} - \chi_{yy})$, $(\chi_{xx} - \chi_{yy})$, and $(\chi_{\alpha\beta} + \chi_{\beta\alpha})$ with $\alpha \neq \beta$ are found to have momentum dependence $2q_z^2 - q_x^2 - q_y^2$, $q_x^2 - q_y^2$, and $q_{\alpha}q_{\beta}$ ($\alpha \neq \beta$) types, respectively, and are special to the cubic noncentrosymmetric case. Along with these the antisymmetric spin fluctuations $i(\chi_{\alpha\beta} - \chi_{\beta\alpha})$ with $\alpha \neq \beta$ with momentum dependence q_{γ} ($\gamma \neq \alpha \neq \beta$) type are also present. A good discussion of the momentum dependence of various spin fluctuations can be found in earlier work³⁴ for the

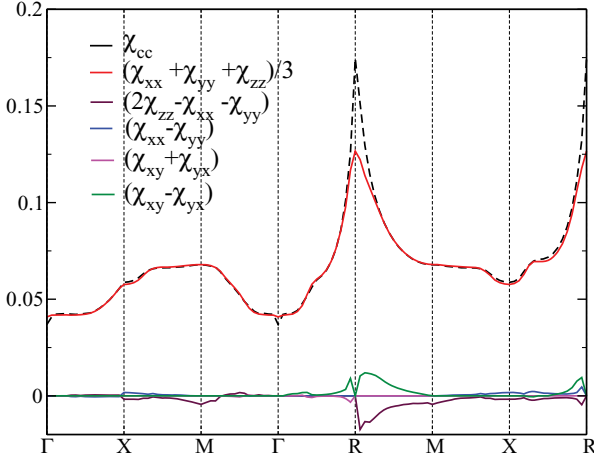


FIG. 3. (Color online) Momentum dependencies as well as the comparison of the relative magnitudes of normal and anomalous spin fluctuations. The charge fluctuation χ_{cc} and normal spin fluctuation $\frac{1}{3}(\chi_{xx} + \chi_{yy} + \chi_{zz})$ contribute strongly compared to the anomalous spin fluctuations. The spin susceptibility also gets enhanced at the R point.

tetragonal NCS case. In Fig. 3 we show the result of numerical calculation of the momentum dependence of various spin fluctuations for our noninteracting model. From this we can also compare the relative strengths of the charge and usual spin fluctuation together with the anomalous spin fluctuations along symmetrical lines. Each spin fluctuation follows the appropriate symmetry of momentum dependence. We observe the largeness of the usual spin fluctuation compared to other symmetric and antisymmetric spin fluctuations. The charge and usual spin fluctuations are enhanced at the nesting vector implying that the system is rather close to an instability.

III. SUPERCONDUCTING GAP EQUATION

In this section we derive the superconducting gap equations and solve them to get the nature and symmetry of the superconducting gap. We will also see how this large nesting affects the superconducting state.

We start with the discussion of the nature of the superconducting gap function in NCSs in general. As shown by the work of Gor'kov and Rashba,⁷ breakdown of the inversion symmetry leads to a gap function which is a mixture of singlet as well as triplet gap functions in the superconducting state. Thus the most general form of the matrix gap function is

$$\hat{\Delta}_{\mathbf{k}} = [\Psi(\mathbf{k})\hat{\sigma}_0 + \mathbf{d}(\mathbf{k}) \cdot \hat{\sigma}] i\hat{\sigma}_y. \quad (9)$$

Here $\Psi(\mathbf{k})$ is the singlet gap function and the triplet \mathbf{d} vector is $\mathbf{d}(\mathbf{k}) = (d_x(\mathbf{k}), d_y(\mathbf{k}), d_z(\mathbf{k}))$. In NCSs the triplet component satisfying $|\mathbf{d}(\mathbf{k}) \cdot \mathbf{g}_{\mathbf{k}}| = |\mathbf{d}(\mathbf{k})||\mathbf{g}_{\mathbf{k}}|$ only survives the pinning from the ASO coupling.⁴⁸ So one can write $\mathbf{d}(\mathbf{k}) = \phi(\mathbf{k})\mathbf{g}_{\mathbf{k}}$ where $\phi(\mathbf{k})$ has the same symmetry of momentum dependence as $\Psi(\mathbf{k})$. With all these we can define the normal $\hat{G}(\mathbf{k}, i\omega_n)$ and anomalous $\hat{F}(\mathbf{k}, i\omega_n)$ matrix Green's functions as given by

$$\hat{G}(\mathbf{k}, i\omega_n) = G_+(\mathbf{k}, i\omega_n)\hat{\sigma}_0 + G_-(\mathbf{k}, i\omega_n)\tilde{\mathbf{g}}_{\mathbf{k}} \cdot \hat{\sigma}, \quad (10)$$

$$\hat{F}(\mathbf{k}, i\omega_n) = [F_+(\mathbf{k}, i\omega_n)\hat{\sigma}_0 + F_-(\mathbf{k}, i\omega_n)\tilde{\mathbf{g}}_{\mathbf{k}} \cdot \hat{\sigma}] i\hat{\sigma}_y. \quad (11)$$

Here $\tilde{\mathbf{g}}_{\mathbf{k}} = \mathbf{g}_{\mathbf{k}}/|\mathbf{g}_{\mathbf{k}}|$. G_{\pm} and F_{\pm} are given as

$$G_{\pm}(\mathbf{k}, i\omega_n) = \frac{1}{2} \left(\frac{-i\omega_n - \varepsilon_{\mathbf{k}+}}{\omega_n^2 + E_{\mathbf{k}+}^2} \pm \frac{-i\omega_n - \varepsilon_{\mathbf{k}-}}{\omega_n^2 + E_{\mathbf{k}-}^2} \right), \quad (12)$$

$$F_{\pm}(\mathbf{k}, i\omega_n) = \frac{1}{2} \left(\frac{\Delta_{\mathbf{k}+}}{\omega_n^2 + E_{\mathbf{k}+}^2} \pm \frac{\Delta_{\mathbf{k}-}}{\omega_n^2 + E_{\mathbf{k}-}^2} \right). \quad (13)$$

Here $\Delta_{\mathbf{k}\pm} = \Psi(\mathbf{k}) \pm \phi(\mathbf{k})|\mathbf{g}_{\mathbf{k}}|$ and $E_{\mathbf{k}\pm} = \sqrt{\varepsilon_{\mathbf{k}\pm}^2 + \Delta_{\mathbf{k}\pm}^2}$.

Our next step is to get the superconducting gap equations. To derive the pairing potential we treat the interaction term H_1 perturbatively and expand the Green's function within the second-order perturbation theory. The gap equations are obtained from the anomalous self-energy part of the expanded Green's function. Details of this procedure are sketched in the Appendix. We follow the standard procedure^{35,49,50} to arrive at the following superconducting gap equation:

$$\begin{aligned} & [\Psi(\mathbf{k})d_x(\mathbf{k})d_y(\mathbf{k})d_z(\mathbf{k})]^t \\ &= \frac{1}{N_0} \sum_{\mathbf{q}} \begin{pmatrix} V_{ss}(\mathbf{q}) & V_{sx}(\mathbf{q}) & V_{sy}(\mathbf{q}) & V_{sz}(\mathbf{q}) \\ V_{xs}(\mathbf{q}) & V_{xx}(\mathbf{q}) & V_{xy}(\mathbf{q}) & V_{xz}(\mathbf{q}) \\ V_{ys}(\mathbf{q}) & V_{yx}(\mathbf{q}) & V_{yy}(\mathbf{q}) & V_{yz}(\mathbf{q}) \\ V_{zs}(\mathbf{q}) & V_{zx}(\mathbf{q}) & V_{zy}(\mathbf{q}) & V_{zz}(\mathbf{q}) \end{pmatrix} \\ & \times \begin{pmatrix} \mathcal{F}_s(\mathbf{k} - \mathbf{q}) \\ \mathcal{F}_x(\mathbf{k} - \mathbf{q}) \\ \mathcal{F}_y(\mathbf{k} - \mathbf{q}) \\ \mathcal{F}_z(\mathbf{k} - \mathbf{q}) \end{pmatrix}. \end{aligned} \quad (14)$$

Here $V_{\zeta\eta}$ with $(\zeta, \eta) = (s, x, y, z)$ denotes the pairing potential arising from the corresponding fluctuation exchange and they are expressed as

$$\begin{aligned} V_{ss}(\mathbf{q}) &= -U - U^2[\chi_{xx}(\mathbf{q}) + \chi_{yy}(\mathbf{q}) + \chi_{zz}(\mathbf{q}) - \chi_{cc}(\mathbf{q})], \\ V_{\zeta\zeta}(\mathbf{q}) &= U^2[\chi_{cc}(\mathbf{q}) + \chi_{\eta\eta}(\mathbf{q}) + \chi_{\delta\delta}(\mathbf{q}) - \chi_{\zeta\zeta}(\mathbf{q})], \\ V_{\zeta\eta}(\mathbf{q}) &= V_{\eta\zeta}(\mathbf{q}) = -U^2[\chi_{\zeta\eta}(\mathbf{q}) + \chi_{\eta\zeta}(\mathbf{q})], \\ V_{s\zeta}(\mathbf{q}) &= -V_{\zeta s}(\mathbf{q}) = iU^2[\chi_{\eta\delta}(\mathbf{q}) - \chi_{\delta\eta}(\mathbf{q})], \end{aligned} \quad (15)$$

where $\zeta \neq \eta \neq \delta$. Here \mathcal{F}_s and \mathcal{F}_{α} are the contributions from the anomalous Green's functions after frequency summation³⁵ and given by

$$\hat{\mathcal{F}}(\mathbf{k}) = [\mathcal{F}_s(k)\hat{\sigma}_0 + \mathcal{F}_{\alpha}(k) \cdot \hat{\sigma}] i\hat{\sigma}_y, \quad (16)$$

where

$$\begin{aligned} \mathcal{F}_s(\mathbf{k}) &= \frac{1}{2} [\psi(\mathbf{k})\phi_+(\mathbf{k}) + \mathbf{d}(\mathbf{k}) \cdot \tilde{\mathbf{g}}_{\mathbf{k}}\phi_-(\mathbf{k})], \\ \mathcal{F}_{\alpha}(\mathbf{k}) &= \frac{\tilde{g}_{\mathbf{k}\alpha}}{2} [\psi(\mathbf{k})\phi_-(\mathbf{k}) + \mathbf{d}(\mathbf{k}) \cdot \tilde{\mathbf{g}}_{\mathbf{k}}\phi_+(\mathbf{k})], \\ \phi_{\pm}(\mathbf{k}) &= \frac{\tanh(E_{\mathbf{k}+}/2T)}{2E_{\mathbf{k}+}} \pm \frac{\tanh(E_{\mathbf{k}-}/2T)}{2E_{\mathbf{k}-}}. \end{aligned} \quad (17)$$

The superconducting gap equation Eq. (14) is actually four coupled equations. Since our main interest is to explain the nature and symmetry of the gap function for this NCS system, we avoid an estimation of the transition temperature T_c from these equations. Instead we fix T_c at $0.02t_1$ and calculate the maximum eigenvalue of the right-hand side of Eq. (14) changing the U value. Figure 4 gives us the critical value of the on-site interaction U for superconductivity, i.e., $U_c = 1.675t_1$, when maximum eigenvalue becomes unity.

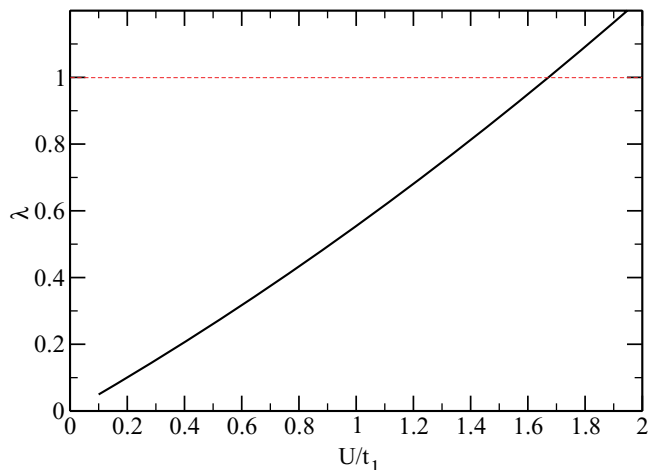


FIG. 4. (Color online) The variation of maximum eigenvalue with U/t_1 . Red dotted line gives us the critical U for $\lambda = 1$.

We thus get the momentum dependence of both singlet and triplet gap functions as the eigenfunctions of the maximum eigenvalue. From the momentum dependence of the gap function we conclude that the superconductivity belongs to the A_1 representation of the point group O .

Finally, we discuss details of the gap function. In our calculation the triplet gap function is found to be a few orders of magnitude smaller than the singlet one, so we extract only the singlet part. In Fig. 5 we present the contour plot of the singlet gap function at three different k_z values in the first Brillouin zone. The singlet gap function changes sign from positive (red) to negative (violet) by gradually moving from Γ to R point and vanishes completely somewhere in between forming the nodal surface. Here we would like to mention that the magnitude of the gap function is largest at either the Γ or R point although the nesting is not so strong here. On the other hand the cagelike portion of the Fermi surface where we have the strongest nesting gives rise to a weak gap function. This can be understood from a careful observation of Eq. (15). The summation of prefactor $\Gamma_{+-}^{\tau\tau}(\mathbf{k}, \mathbf{Q})$ of charge and spin susceptibility $\chi_{\tau\tau}(\mathbf{Q})$ vanishes for the spin-singlet pairing potential $V_{ss}(\mathbf{Q})$ at the nesting vector $\mathbf{Q} = (\pi, \pi, \pi)$. Because of this, even strong interband nesting does not play any role in opening up the gap function. However, the pairing potential forms the gap on the Fermi surfaces around the Γ and R points, connected by subdominant nesting of $\chi_{++}(\mathbf{Q})$ and $\chi_{--}(\mathbf{Q})$. Thus the singlet gap function with opposite

signs between these points opens up and a curved surface of closing-gap momentum can exist in between. In this figure we show the positive helicity Fermi surface by the + sign and the dotted line denotes the exact location where the gap function vanishes. In Fig. 5(c) we encounter the maximum negative value of the gap function at the corner R points. In Fig. 5(a) the gap is positive maximum. In Fig. 5(b), we can find the intersection between the Fermi surface and the surface of the closing-gap momentum, corresponding to “the line node” of the gap function. Since the representation of superconductivity is A_1 the line node is an accidental one, which is not protected by symmetry, but rather depends on the three-dimensional geometry of the Fermi surface. Thus the gap function appears to be singlet s_{\pm} type with accidental line nodes.

IV. SURFACE BOUND STATES

In this section we mainly discuss two topics. The first one is related to the nodal structure of the gap function for both positive as well as negative helicity bands. Next we discuss the novel topological aspects of the nodal lines (that are present in this system) related to the edge states. To begin with we show the three-dimensional structures of gap functions on both helicity Fermi surfaces in Fig. 6. Usually we can identify the line nodes from the intersection between the Fermi surface of certain helicity bands and the nodal contour of the same helicity gap function. Using this method we identify the location of the line nodes both for the negative helicity band in Fig. 6(a) as well as for the positive helicity band in Fig. 6(b).

Following the recent categorization of the topological surface states for nodal²⁹⁻³² noncentrosymmetric superconductors we find it worthy to discuss our case. The nodal lines in the bulk of the noncentrosymmetric superconductor can give rise to the zero-energy surface bound states which appear only in some closed regions bounded by the projections of the closed nodal lines of the bulk gap. The zero-energy surface states have some distinct topological origin and give rise to a zero-bias tunneling conductance peak.

According to the existing literature the nontrivial value of the topological invariant $W_{[lmn]}$ ²⁹⁻³² leads to the surface flat bands and can be observed in the surface spectral function for a suitably chosen surface with the normal along $[lmn]$. The topological invariant $W_{[lmn]}$ is defined by the equation

$$W_{[lmn]}(\mathbf{k}_{\parallel}) = -\frac{1}{2} \sum_{\nu=\pm} [\text{sgn}(\Delta_{\mathbf{k}_F, \nu}^{\nu}) - \text{sgn}(\Delta_{\mathbf{k}_F, \nu}^{\nu})], \quad (18)$$

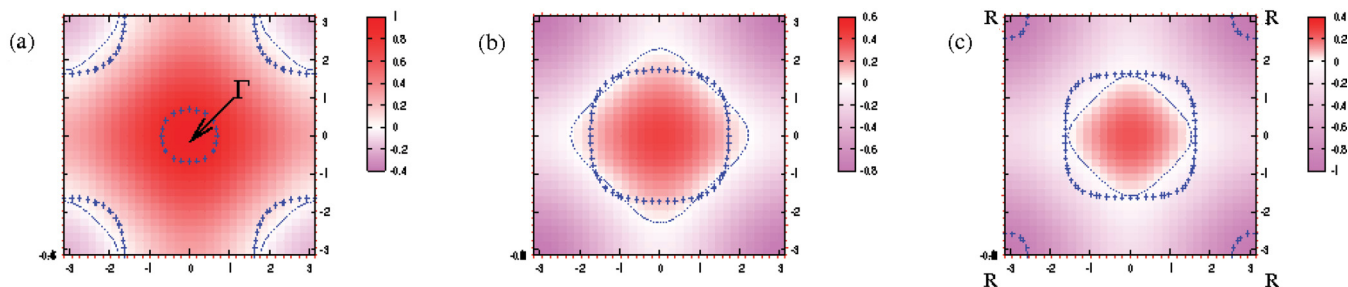


FIG. 5. (Color online) The contour plot of the singlet gap function at three k_z values: (a) $k_z = 0.0$, (b) $k_z = 0.7\pi$, and (c) $k_z = \pi$. Gap function varies from positive maximum (red) to the negative maximum (violet) following the scale attached to each figure. The blue line with + sign shows the Fermi surface of the positive helicity band while the dotted blue line denotes the nodes of the gap function (details in text).

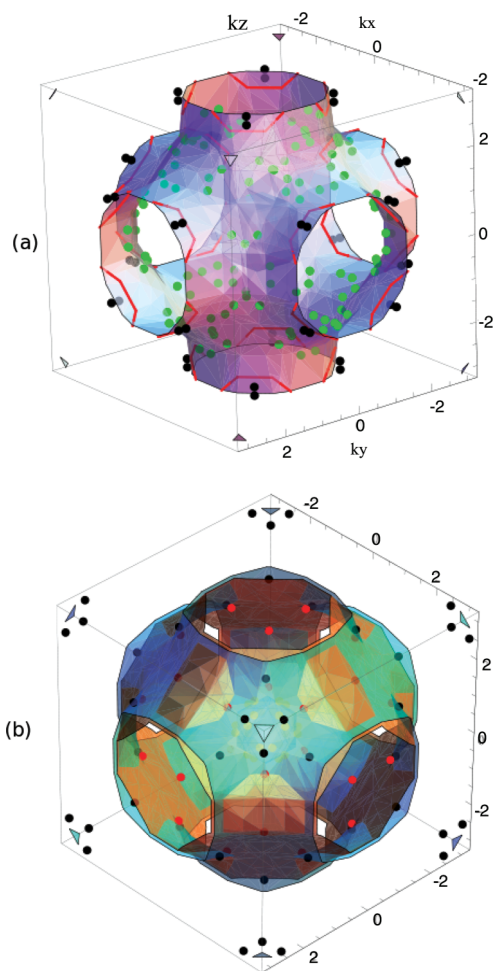


FIG. 6. (Color online) (a) Fermi surface of the negative helicity band in the first Brillouin zone. The nodal lines of the gap function (shown in red lines) are located near the edge of the mouths of the Fermi surface. Surrounding each mouth there exist two pairs of nodal lines. The green (black) dots denote the region where the sign of the gap function is positive (negative) on the negative helicity Fermi surface. (b) The same for positive helicity band where the dots have the same meaning. Now we show orange patches on the Fermi surface which actually have a positive sign of the gap function surrounded by the negative sign region (blue region with occasional black dots). Thus the boundary between them give rise to the line nodes of this gap function. There are four such patches surrounding each mouth and each patch is shared by two mouths of the positive helicity Fermi surface, totaling twelve in number.

where $\mathbf{k}_{F,v}$ ($\tilde{\mathbf{k}}_{F,v}$) are vectors located on the helicity Fermi surface v , which decomposes into a component parallel to $[lmn]$ and a two-dimensional vector \mathbf{k}_{\parallel} on the $[lmn]$ plane (common between $\mathbf{k}_{F,v}$ and $\tilde{\mathbf{k}}_{F,v}$).

To start with we consider the case for a spherical Fermi surface. For a spherical Fermi surface the line of integration [in the sense of Eq. (14) in Ref. 32] always crosses the Fermi surface twice, making it possible to define a $\tilde{\mathbf{k}}$ for every \mathbf{k} as defined in Eq. (18) for any $[lmn]$. In our case the shape of the Fermi surface vastly differs from the spherical one, especially near the mouth region of the Fermi surface, as shown in Fig. 6, where the nodal rings are located. Here first the nodal

lines do not form a closed loop. Second, we cannot define a path of integration simultaneously passing through one region bounded by the nodal rings and another region of a Fermi surface, when we fix the direction along $[111]$.

Since the location of the nodal lines for the negative helicity gap function is different from that of the positive helicity gap function, we have to consider them separately. First we discuss the situation that arises from the negative helicity gap function and will come back to case for positive helicity gap function. To show that the nodal lines indeed form closed loops we repeat our first Brillouin zone along the positive k_z direction. This clearly shows the formation of four nodal rings surrounding each mouth around $k_z = \pi$ in Fig. 7(a). In order to consider the $[111]$ surface we use the equivalent cylindrical hexagonal Brillouin zone and extend the data of the gap function up to the second Brillouin zone, as shown in Fig. 7(b). Now in the effective cylindrical Brillouin zone the nodal lines form closed nodal rings and we can also define the path of the integration which now intersect another part of the Fermi surface after passing through the regions bounded by the nodal rings, so that Eq. (18) can be safely applied. In Fig. 7(c) we draw the projection of Fig. 7(b) on the $[111]$ surface. This figure shows six nodal rings (large black region surrounded by red dots) around corners of the hexagonal Brillouin zone. These six regions are basically the projection of the nodal rings of the bulk gaps as shown in Fig. 7(a). Three of these regions like the top corner in Fig. 7(c) are covered from above by the positive region of the negative helicity gap function. Thus when we consider the path of integration along $[111]$ through these regions, $\mathbf{k}_{F,v}$ lies on the positive sign of the gap function but $\tilde{\mathbf{k}}_{F,v}$ is on the negative sign of gap function giving rise to $W_{[111]}^{v=-} = -1$. On the other hand the other three projected nodal regions are covered from below by the positive-sign region of the negative helicity gap function; thus the reverse is the case. The same consideration gives $W_{[111]}^{v=-} = 1$ for the later three regions. Thus we have six regions with alternate values of $W_{[111]}^{v=\pm} = \pm 1$ as shown in Fig. 7(c).

Similar consideration for positive helicity band gives rise to opposite signs of $W_{[111]}^{v=+}$ as shown in Fig. 8. According to Eq. (18), adding them up results in mutual cancellation of the winding number between two helicity bands. Such cancellation however is not complete (depending on the band structure specific to the actual material) and we can get topologically protected surface states in regions where the cancellation is incomplete. So there is a possibility that the projected regions of the nodal rings give rise to topologically protected zero-energy surface bands.

V. DISCUSSION AND SUMMARY

We thus explained the role of the correlation effect and nesting in the compound $\text{Li}_2\text{Pt}_3\text{B}$ which is responsible for the nodal gap function. The appearance of line nodes as suggested in many experiments is thus explained. This correlation effect is completely absent in the Pd compound. This also explains that if one gradually starts doping the Pd compound with Pt then this correlation effect comes into play gradually and causes the appearance of nodal behavior in the superconducting order parameter at some point. In this

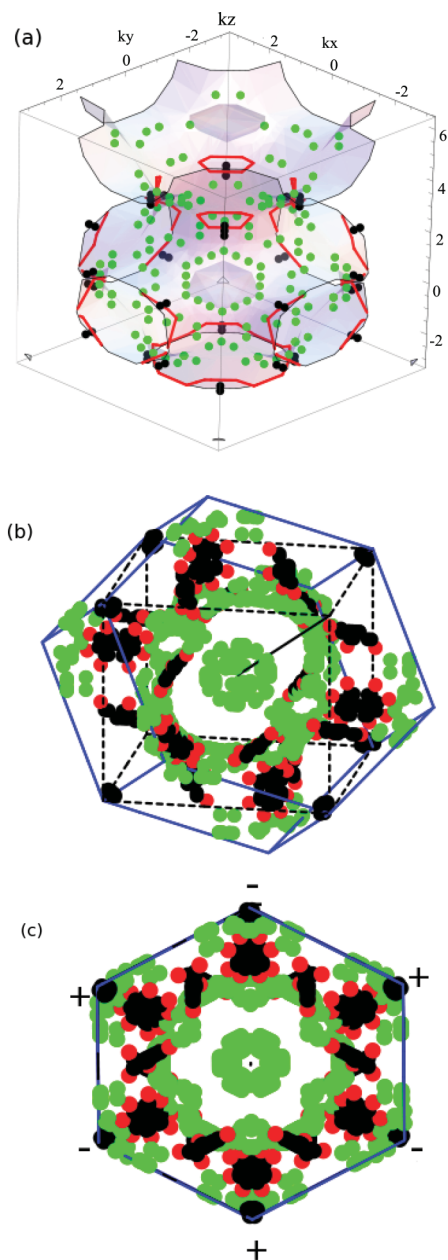


FIG. 7. (Color online) (a) The negative helicity Fermi surface with the negative helicity gap function repeated along the k_z direction. This diagram clearly shows the location of the nodal rings of the gap function. (b) The hexagonal cylinder represents the deformed first Brillouin zone having the same volume as that of the original first Brillouin zone. The first Brillouin zone is also shown with dashed black lines. Few data points are coming from the second Brillouin zone region but included within the cylindrical region. (c) The same diagram as in (b) but projected on [111] surface. Six regions of negative gap function bounded by nodal lines (red dots form closed nodal rings) are clearly visible. These six regions are the projections of the nodal rings of the bulk gap on the [111] surface. The + and - signs indicate the sign of the winding number $W_{[111]}^{v=-}$ at those specific regions.

concluding section we calculate the temperature dependence of the susceptibility in the superconducting state to compare the NMR data. As we have already mentioned the NMR Knight

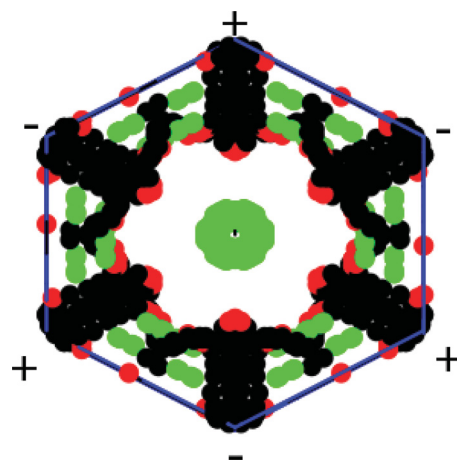


FIG. 8. (Color online) Gap function sign on the positive helicity Fermi surface projected on the [111] surface. Here we have opposite sign of $W_{[111]}^{v=+}$ around the corner when compared with Fig. 7(c).

shift³⁹ experiment gives the temperature-independent Knight shift, which was taken as a signature of spin-triplet Cooper pairing in the superconducting state. Within our scenario since the spin-triplet component is really suppressed, so such a temperature-independent Knight shift is not expected. However we calculate the temperature dependence of the susceptibility and predict a scenario which can explain this temperature-independent Knight shift even for our singlet-dominated superconducting state. Within the weak-coupling approximation neglecting the feedback effect we assume that the order parameter below T_c follows the BCS temperature dependence $\hat{\Delta}(\mathbf{k}, T) = \hat{\Delta}(\mathbf{k}, 0) \tanh(1.74\sqrt{T_c/T - 1})$ at every momentum point. Using this gap function we calculate the uniform susceptibility $\chi_s(T)$ below T_c as follows:¹³

$$\begin{aligned} \chi_s(T) &= (1/3) \sum_{\alpha} \chi_{\alpha\alpha}(T), \\ \chi_{\alpha\beta}(T) &= -\mu_B^2 k_B T \sum_{\mathbf{k}} \sum_{\omega_n} \text{tr}[\hat{\sigma}_{\alpha} \hat{G}(\mathbf{k}, \omega_n) \hat{\sigma}_{\beta} \hat{G}(\mathbf{k}, \omega_n) \\ &\quad - \hat{\sigma}_{\alpha} \hat{F}(\mathbf{k}, \omega_n) \hat{\sigma}_{\beta} \hat{F}^{\dagger}(\mathbf{k}, \omega_n)]. \end{aligned} \quad (19)$$

Here $\chi_{\alpha\beta}(T)$ is the $\alpha\beta$ -component of the temperature-dependent susceptibility in the superconducting state. We carry out the frequency summation and after regrouping terms we arrive at the following equation,

$$\chi_s(T) = \sum_{\mathbf{k}} [\chi_0(\mathbf{k}, T) + \chi_+(\mathbf{k}, T) + \chi_-(\mathbf{k}, T)], \quad (20)$$

where $\chi_0(\mathbf{k}, T)$, $\chi_+(\mathbf{k}, T)$, and $\chi_-(\mathbf{k}, T)$ are given as

$$\begin{aligned} \chi_0(\mathbf{k}, T) &= \frac{1}{3} \sum_{\xi=\pm} \left[\left(1 - \xi \frac{\Delta_{\mathbf{k}+} \Delta_{\mathbf{k}-} + \epsilon_{\mathbf{k}+} \epsilon_{\mathbf{k}-}}{E_{\mathbf{k}+} E_{\mathbf{k}-}} \right) \right. \\ &\quad \times \left. \left(\frac{\tanh\left(\frac{E_{\mathbf{k}+}}{2T}\right) + \xi \tanh\left(\frac{E_{\mathbf{k}-}}{2T}\right)}{E_{\mathbf{k}+} + \xi E_{\mathbf{k}-}} \right) \right], \end{aligned} \quad (21)$$

$$\chi_{\pm}(\mathbf{k}, T) = 1/[12T \cosh^2(E_{\mathbf{k}\pm}/2T)]. \quad (22)$$

We plot in Fig. 9 the contribution from the temperature-independent Van Vleck term $\chi_0(T)$, temperature-dependent

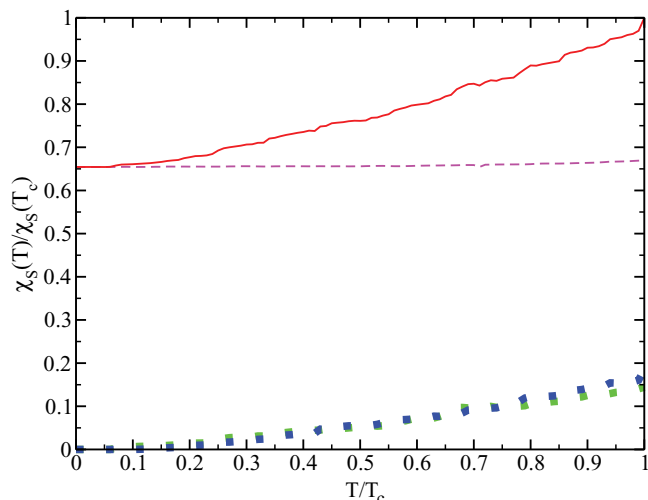


FIG. 9. (Color online) The variation of normalized spin susceptibility (solid red line) with temperature in the superconducting state. Also shown in the same figure are the contributions from the Van Vleck term (dashed magenta line) and the Pauli term of positive helicity band (green square) and negative helicity band (blue square), all scaled by $\chi_s(T_c)$.

Pauli terms $\chi_+(T), \chi_-(T)$, and the susceptibility $\chi_s(T)$ all normalized by $\chi_s(T_c)$ (red line). Although $\chi_s(T)/\chi_s(T_c)$ shows excellent agreement with earlier work,²⁰ it apparently contradicts the NMR Knight shift data.³⁹ It is well known that the Knight shift becomes temperature independent, when the set of the \mathbf{d} vector around the Fermi surface is perpendicular to the magnetic field. So in the present case, the temperature independence cannot be explained even if we start with a triplet-dominant order parameter, since in that case we cannot fix the direction of the magnetic field perpendicular to the \mathbf{d} vector [$\mathbf{d}(\mathbf{k}) \parallel \mathbf{g}_k$]. So neither spin-singlet nor spin-triplet scenario can in fact explain the observed temperature independence in Knight shift data. However to resolve this contradiction, one can formulate a multi-orbital theory which captures the complicated band structure in more detail. Then the large contributions of the Van Vleck term between the t_{2g} and e_g orbitals for a cubic system through spin-orbit interaction is expected and this will further reduce the deviation of the normalized susceptibility from the normal state below T_c . We do not address this issue here.

In conclusion, we suggest that in the noncentrosymmetric superconductor $\text{Li}_2\text{Pt}_3\text{B}$ the considerable d character of the bands near the Fermi energy and nesting of the Fermi surfaces give rise to a weak correlation effect which can be treated perturbatively and this gives rise to a singlet-dominated (with negligible triplet component) s_{\pm} kind of gap function with accidental line nodes arising from the Fermi surface geometry. The three-dimensional geometry of the Fermi surface and the nesting of the Fermi surface play a crucial role in determining the nature of the gap function. We propose that angle-resolved photoemission spectroscopy and de Hass–van Alphen effect experiments may shed light on this nesting property of the Fermi surface and can be useful to study the properties of the superconducting state as well. We also calculate the susceptibility below T_c and emphasize the importance

of the orbital degeneracy of the d electron to explain the experimental data. We also show that the nodal rings of both positive and negative helicity gap functions give rise to some nontrivial winding numbers with opposite signs between the two bands and the winding numbers cancel partially. Thus, momentum regions having totally nontrivial winding number corresponding to topologically protected surface flat bands appear in the surface Brillouin zone depending on the direction of surface and the superconducting electronic states, even though the gap function is singlet dominating.

ACKNOWLEDGMENTS

The authors are grateful to Y. Yanase and M. Sato for fruitful, stimulating discussions during their visit to the Asia Pacific Center for Theoretical Physics (APCTP). We acknowledge the Max Planck Society (MPG), the Korea Ministry of Education, Science, and Technology (MEST), Gyeongsangbuk-Do, and Pohang City for the support of the Independent Junior Research Groups at APCTP. T.T. acknowledges the support by the National Research Foundation of Korea (NRF) funded by the Ministry of Education, Science, and Technology (Grant No. 2012R1A1A2008559).

APPENDIX: DERIVATION OF EQUATION (14)

Within the weak-coupling theory of superconductivity only static susceptibility is required for calculating the superconducting gap equations and we have already derived them in the last part of Sec. II. The static susceptibilities $\chi_{\alpha\beta}(\mathbf{q})$ are transformed to $\chi_{\sigma_1\sigma_2\sigma_3\sigma_4}(\mathbf{q})$ as

$$\begin{pmatrix} \chi_{ss}(\mathbf{q}) & \chi_{sz}(\mathbf{q}) & \chi_{sx}(\mathbf{q}) & \chi_{sy}(\mathbf{q}) \\ \chi_{zs}(\mathbf{q}) & \chi_{zz}(\mathbf{q}) & \chi_{zx}(\mathbf{q}) & \chi_{zy}(\mathbf{q}) \\ \chi_{xs}(\mathbf{q}) & \chi_{xz}(\mathbf{q}) & \chi_{xx}(\mathbf{q}) & \chi_{xy}(\mathbf{q}) \\ \chi_{ys}(\mathbf{q}) & \chi_{yz}(\mathbf{q}) & \chi_{yx}(\mathbf{q}) & \chi_{yy}(\mathbf{q}) \end{pmatrix} = \frac{1}{2} \hat{W} \begin{pmatrix} \chi_{\uparrow\uparrow\uparrow\uparrow}(\mathbf{q}) & \chi_{\uparrow\uparrow\downarrow\downarrow}(\mathbf{q}) & \chi_{\uparrow\uparrow\uparrow\downarrow}(\mathbf{q}) & \chi_{\uparrow\uparrow\downarrow\uparrow}(\mathbf{q}) \\ \chi_{\downarrow\downarrow\uparrow\uparrow}(\mathbf{q}) & \chi_{\downarrow\downarrow\downarrow\downarrow}(\mathbf{q}) & \chi_{\downarrow\downarrow\uparrow\downarrow}(\mathbf{q}) & \chi_{\downarrow\downarrow\downarrow\uparrow}(\mathbf{q}) \\ \chi_{\uparrow\downarrow\uparrow\uparrow}(\mathbf{q}) & \chi_{\uparrow\downarrow\downarrow\downarrow}(\mathbf{q}) & \chi_{\uparrow\downarrow\uparrow\downarrow}(\mathbf{q}) & \chi_{\uparrow\downarrow\downarrow\uparrow}(\mathbf{q}) \\ \chi_{\downarrow\uparrow\uparrow\uparrow}(\mathbf{q}) & \chi_{\downarrow\uparrow\downarrow\downarrow}(\mathbf{q}) & \chi_{\downarrow\uparrow\uparrow\downarrow}(\mathbf{q}) & \chi_{\downarrow\uparrow\downarrow\uparrow}(\mathbf{q}) \end{pmatrix} \hat{W}^\dagger. \quad (\text{A1})$$

Here \hat{W} is the orthogonal matrix of transformation given as

$$\hat{W} = \begin{pmatrix} 1 & 1 & 0 & 0 \\ 1 & -1 & 0 & 0 \\ 0 & 0 & 1 & i \\ 0 & 0 & 1 & -i \end{pmatrix}, \quad (\text{A2})$$

and $\chi_{\sigma_1\sigma_2\sigma_3\sigma_4}(\mathbf{q})$ is defined as

$$\chi_{\sigma_1\sigma_2\sigma_3\sigma_4}(\mathbf{q}) = -T \sum_{\mathbf{k}} \sum_m G_{\sigma_3\sigma_1}(\mathbf{k}, i\omega_m) G_{\sigma_2\sigma_4}(\mathbf{k} + \mathbf{q}, i\omega_m). \quad (\text{A3})$$

Now we expand the superconducting normal Green's function within the weak-coupling approach treating H_1 as a

perturbation term. We find the contribution to the self-energy which give us the gap equations. Following this procedure we can write the gap equation in spin space as

$$\Delta_{\sigma_1\sigma_2} = \chi_{\sigma_1\sigma_2}\mathcal{F}_{\sigma_1\sigma_2} - \chi_{\bar{\sigma}_1\bar{\sigma}_2}\mathcal{F}_{\bar{\sigma}_1\bar{\sigma}_2} - \chi_{\sigma_1\bar{\sigma}_2}\mathcal{F}_{\sigma_1\bar{\sigma}_2} + \chi_{\bar{\sigma}_1\sigma_2}\mathcal{F}_{\bar{\sigma}_1\sigma_2}. \quad (\text{A4})$$

Here $\mathcal{F}_{\sigma_1\sigma_2}$ are the components of the matrix anomalous Green's function. In Eq. (A4) the first term is the contribution from the first Feynman diagram in Fig. 10 and the last three terms are three different contributions from the other Feynman diagram. Simultaneously using Eqs. (9), (16), and (A1) in Eq. (A4) we arrive at the gap equation Eq. (14).

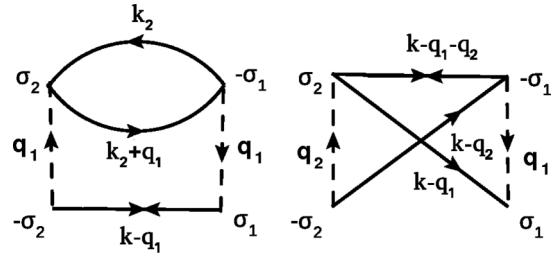


FIG. 10. Feynman diagrams that contribute to the gap function. Here $-\sigma = \bar{\sigma}$, i.e., spin opposite to that of σ . The solid single line represents the electronic line and the dashed line represents the interaction line. The double arrow indicates the anomalous Green's function.

- ¹S. Sachdev, *Phys. Status Solidi B* **247**, 537 (2010).
- ²D. J. Scalapino, E. Loh, Jr., and J. E. Hirsch, *Phys. Rev. B* **34**, 8190 (1986).
- ³N. D. Mathur, F. M. Grosche, S. R. Julian, I. R. Walker, D. M. Freye, R. K. W. Haselwimmer, and G. G. Lonzarich, *Nature (London)* **394**, 39 (1998).
- ⁴J. E. Hirsch, *Phys. Rev. Lett.* **54**, 1317 (1985).
- ⁵K. Miyake, S. Schmitt-Rink, and C. M. Varma, *Phys. Rev. B* **34**, 6554 (1986).
- ⁶E. Bauer, G. Hilscher, H. Michor, Ch. Paul, E. W. Scheidt, A. Gribanov, Yu. Seropugin, H. Noël, M. Sigrist, and P. Rogl, *Phys. Rev. Lett.* **92**, 027003 (2004).
- ⁷L. P. Gor'kov and E. I. Rashba, *Phys. Rev. Lett.* **87**, 037004 (2001).
- ⁸N. Hiasa and R. Ikeda, *Phys. Rev. B* **78**, 224514 (2008).
- ⁹K. V. Samokhin, *Phys. Rev. B* **78**, 224520 (2008).
- ¹⁰Y. Tada, N. Kawakami, and S. Fujimoto, *Phys. Rev. Lett.* **101**, 267006 (2008).
- ¹¹K. V. Samokhin, *Phys. Rev. Lett.* **94**, 027004 (2005).
- ¹²V. P. Mineev, *Phys. Rev. B* **71**, 012509 (2005).
- ¹³P. A. Frigeri, D. F. Agterberg, and M. Sigrist, *New J. Phys.* **6**, 115 (2004).
- ¹⁴K. Børkje and A. Sudbø, *Phys. Rev. B* **74**, 054506 (2006).
- ¹⁵S. S. Mandal and S. P. Mukherjee, *J. Phys.: Condens. Matter* **18**, L593 (2006).
- ¹⁶T. Yokoyama, Y. Tanaka, and J. Inoue, *Phys. Rev. B* **72**, 220504(R) (2005).
- ¹⁷J. Linder and A. Sudbø, *Phys. Rev. B* **76**, 054511 (2007).
- ¹⁸S. Wu and K. V. Samokhin, *Phys. Rev. B* **80**, 014516 (2009).
- ¹⁹V. P. Mineev and K. V. Samokhin, *Phys. Rev. B* **75**, 184529 (2007).
- ²⁰K. V. Samokhin, *Phys. Rev. B* **76**, 094516 (2007).
- ²¹B. Liu and I. Eremin, *Phys. Rev. B* **78**, 014518 (2008).
- ²²K. V. Samokhin, *Phys. Rev. B* **78**, 144511 (2008).
- ²³C. Iniotakis, N. Hayashi, Y. Sawa, T. Yokoyama, U. May, Y. Tanaka, and M. Sigrist, *Phys. Rev. B* **76**, 012501 (2007).
- ²⁴S. P. Mukherjee and S. S. Mandal, *J. Phys.: Condens. Matter* **21**, 375702 (2009).
- ²⁵S. P. Mukherjee, *Eur. Phys. J. B* **80**, 51 (2011).
- ²⁶Y. Tanaka, T. Yokoyama, A. V. Balatsky, and N. Nagaosa, *Phys. Rev. B* **79**, 060505(R) (2009).
- ²⁷S. Fujimoto, *Phys. Rev. B* **77**, 220501(R) (2008).
- ²⁸M. Sato and S. Fujimoto, *Phys. Rev. B* **79**, 094504 (2009).
- ²⁹A. P. Schnyder and S. Ryu, *Phys. Rev. B* **84**, 060504(R) (2011).
- ³⁰T. T. Heikkila, N. B. Kopnin, and G. E. Volovik, *JETP Lett.* **94**, 233 (2011).
- ³¹M. Sato, Y. Tanaka, K. Yada, and T. Yokoyama, *Phys. Rev. B* **83**, 224511 (2011).
- ³²A. P. Schnyder, P. M. R. Brydon, and Carsten Timm, *Phys. Rev. B* **85**, 024522 (2012).
- ³³Y. Yanase and M. Sigrist, *J. Phys. Soc. Jpn.* **76**, 124709 (2007).
- ³⁴T. Takimoto, *J. Phys. Soc. Jpn.* **77**, 113706 (2008).
- ³⁵T. Takimoto and P. Thalmeier, *J. Phys. Soc. Jpn.* **78**, 103703 (2009).
- ³⁶K. Togano, P. Badica, Y. Nakamori, S. Orimo, H. Takeya, and K. Hirata, *Phys. Rev. Lett.* **93**, 247004 (2004).
- ³⁷P. Badica, T. Kondo, and K. Togano, *J. Phys. Soc. Jpn.* **74**, 1014 (2005).
- ³⁸M. Nishiyama, Y. Inada, and G.-Q. Zheng, *Phys. Rev. B* **71**, 220505(R) (2005).
- ³⁹M. Nishiyama, Y. Inada, and G.-Q. Zheng, *Phys. Rev. Lett.* **98**, 047002 (2007).
- ⁴⁰H. Takeya, K. Hirata, K. Yamaura, K. Togano, M. El Massalami, R. Rapp, F. A. Chaves, and B. Ouladdiaf, *Phys. Rev. B* **72**, 104506 (2005).
- ⁴¹H. Takeya, M. El Massalami, S. Kasahara, and K. Hirata, *Phys. Rev. B* **76**, 104506 (2007).
- ⁴²P. S. Häfliger *et al.*, *J. Supercond. Nov. Magn.* **22**, 337 (2009).
- ⁴³H. Q. Yuan, D. F. Agterberg, N. Hayashi, P. Badica, D. Vandervelde, K. Togano, M. Sigrist, and M. B. Salamon, *Phys. Rev. Lett.* **97**, 017006 (2006).
- ⁴⁴T. Yokoyama, T. Muro, I. Hase, H. Takeya, K. Hirata, and K. Togano, *Phys. Rev. B* **71**, 092507 (2005).
- ⁴⁵S. Chandra, S. Mathi Jaya, and M. C. Valsakumar, *Physica C* **432**, 116 (2005).
- ⁴⁶K.-W. Lee and W. E. Pickett, *Phys. Rev. B* **72**, 174505 (2005).
- ⁴⁷K. V. Samokhin and V. P. Mineev, *Phys. Rev. B* **77**, 104520 (2008).
- ⁴⁸P. A. Frigeri, D. F. Agterberg, A. Koga, and M. Sigrist, *Phys. Rev. Lett.* **92**, 097001 (2004).
- ⁴⁹Y. Tada, N. Kawakami, and S. Fujimoto, *J. Phys. Soc. Jpn.* **77**, 054707 (2008).
- ⁵⁰Y. Yanase and M. Sigrist, *J. Phys. Soc. Jpn.* **77**, 124711 (2008).